Electronic Supplementary Material (ESI) for Nanoscale.

Updated supplementary information for c8nr01659c, the revised parts are highlighted in yellow background.

Supplementary Information

High-density deformation nanotwin induced significant improvement in the plasticity of polycrystalline γ-TiAl-based intermetallic alloys

Shiqiu Liu, Hongsheng Ding, Hailong Zhang, Ruirun Chen, Jingjie Guo, Hengzhi Fu*

National Key Laboratory for Precision Hot Processing of Metals, School of Materials Science and Engineering, P. O. Box 434, Harbin Institute of Technology, Harbin 150001, China

*To whom correspondence should be addressed; E-mail: dinghsh@hit.edu.cn

Contents

Methods

The continuous casting of the master alloy was carried out by an electromagnetic cold crucible (EMCC) multifunctional continuous casting equipment set up by our research group, whose schematic diagram is shown in Figure S1 and the detailed operating procedures can refer to ref. (*1*).

Microstructure and phase evolution of as-cast Ti-45.5Al-4Cr-2.5Nb alloy during anneal at 1250 ℃

When the as-cast alloy was annealed at 1250℃ for 1 hour, the microsegregation degree was reduced dramatically in comparison to the as-cast alloy (Figure S2a), whereas the Al-segregation can also be distinguished in the ILC area. With the annealing time increased, the microsegregation was relieved further. It can be observed that the microsegregation is almost canceled in the sample S2 (Figure S2d), and its microstructures are more homogeneous than those of sample S1.

In order to disclose the phase evolution process of the as-cast alloy during annealing at 1250 ℃, XRD examinations were carried out to the as-cast and annealed alloys, the XRD patterns are shown in Figure S3. According to the patterns, although all of the three alloys mainly consist of γ, B2 and α_2 phase, the content of each constituent phase has significant distinction among the three alloys, as indicated by the variation of the relative intensity of corresponding diffraction peaks. At first, both the position and intensity of the dominant diffraction peak are changed with the annealing time increased. Specifically, the dominant diffraction peak of the as-cast alloy corresponds to γ phase, while that of the two as-annealed

alloys is identified as coming from γ/α_2 lamellar structure; and the intensity of the dominant peak improves with the increase of annealing time (here the as-cast alloy is regarded as being annealed at 1250 ℃ for 0 hour). These results indicate that there are exactly few γ/α_2 lamellar structures in the as-cast alloy as shown in Figure 1; moreover, after the as-cast alloy was annealed at 1250 ℃ for 1 ~ 2 hours, γ/α_2 lamellar structures were generated and their content increased with the increase of annealing time. At second, the intensity of other diffraction peaks varies with the annealing time increased. The (110) B2 peak is the main diffraction peak of B2 phase, its intensity decreases firstly and then increases with the annealing time increased, which can reflect the corresponding variation trend of the B2 phase content. The intensity variation trends with respect to different γ phase diffraction peaks are not completely consistent, such as the intensity variation trends of (202), (220), (110) and (001), (002), (200) crystal planes, it is revealed that both the decomposition and growth process of γ phase coexisted in the investigated alloy during annealing. At last, as shown in Figure S3c, there is a weak diffraction peak at 2θ=28.13° detected in sample S2. After careful identification, it's found this peak match with the (015) crystal plane of η-$TiAl_2$ phase well. Due to the fact that only when the Al element of γ phase is more than 55 at. % can η-$TiAl_2$ phase precipitate from it at low temperature, while the average Al content of γ phase in as-cast alloy is 48.73 at. % (as shown in Table S1), then it's really unusual of this phenomenon. What can be inferred is that local Al element enrichment and/or lattice defects generated during annealing promoted the precipitation of η-$TiAl_2$ phase, however, the specific reasons need be further investigated.

By performing Rietveld refinement to XRD patterns, lattice parameters and weight percentage of each constituent phase in as-cast and annealed Ti-45.5Al-4Cr-2.5Nb alloys were achieved (as shown in Table S2). According to the XRD refinement results, the γ phase content decreased

with the increase of annealing time, while the α_2 phase content had the reverse variation trend; the B2 phase content decreased firstly and then increased with the annealing time increasing, which is exactly consistent with the change law of peak intensity. With respect to the lattice parameters of each constituent phase, the *c*/*a* ratio of γ phase approached to a stable value with the annealing time increasing, which indicates the γ phase changed from a metastable state to stable one during annealing. Besides, the lattice parameter of B2 phase continuously increased with the annealing time increasing, which is thought as resulting from the content increase of big-size atom (Ti) and the content decrease of small-size atoms (Cr, Al) in crystal cell (Table S1). On basis of the above XRD analysis, the evolution rule of each constituent phase with the annealing time is approximately made clear.

In order to further know about the microstructure evolution process of the as-cast alloy during annealing, a number of high magnification BSE images from the two as-annealed alloys were investigated particularly. Figure S2b shows the typical ILC area microstructures in sample S1. Compared with those in the as-cast alloy, two differences can be distinguished easily. The first one is that the long rod-like γ phases (average 18.45 μm in length and 5.82 μm in width) changed into short rod-like or round ones (11.74 μm in equivalent diameter) after annealed, namely spheroidizing phenomenon of the rod-like γ phase. The second one is that a lot of granular grey phases were generated adjacent to blocky γ phase. The grey phases can be identified as α_2 phase by XRD and EDS analysis. Figure S2e is the typical ILC area microstructures in sample S2, their appearance is similar to that in sample S1. In spite of the similarity, the shape of γ phase became more uniform and rounder (the size changes little, about 11.99 μm), and more granular α_2 phases were generated in the sample S2. By making numerous statistics, it's found that the diameter of granular α_2 phase increased from 6.86 μm to 8.54 μm with the annealing time increasing from 1

to 2 hours. Figure S2c and f present typical lamellar structures in sample S1 and S2, respectively, both of which mainly consist of α_2/γ lamellae. There remain some B2 pieces in the lamellar structures of sample S1, while few B2 lamellae can be observed in those of sample S2. It's indicated that the B2 phase in lamellar structures continuously decomposed with the annealing time increasing. However, by comparing the B2 phase in ILC area between sample S1 and S2, it's observed that the B2 content for sample S2 is more than that for sample S1. Combined with the XRD refinement results, the evolution rule of B2 phase during annealing can be reconstructed. With the beginning of anneal at 1250 ℃, the B2 phase, mainly the B2 lamellae, started to decompose, which resulted in the slight decrease of B2 content after the as-cast alloy was annealed for 1 hour. With the annealing time increasing, the B2 phase in lamellar structures almost decomposed completely, while that in ILC area grew up gradually, this is why the B2 phase content increased in turn when the annealing time increased to 2 hours. The microstructure observation further verifies the XRD analysis results about the evolution rule of each constituent phase in investigated alloy during annealing.

Figure S4 shows the representative TEM bright-field images from sample S1. By analyzing these pictures, it's able to know about the microstructure evolution of as-cast alloy during annealing more clearly, especially for the lamellar structures. As revealed by Figure S4a, the γ/γ lamellae transformed into α_2/γ lamellae during annealing through α_2 lamellae precipitating between γ lamellae. There are numerous dislocations at the γ/γ interface in as-cast alloy (Figure 1), they could provide beneficial conditions for the nucleation of α_2 lamellae. Figure S4b shows the morphology of α_2/γ lamellar structures transformed incompletely. There are some thin B2 lamellae (~ 90 nm) retained in the γ lamellae, they are evidently thinner than those (300 ~ 400 nm) in the as-cast alloy, it's indicated that the B2 lamellae were dissolved into the γ lamellae

when annealed at 1250 ℃. Besides, an obvious interface is observed in a γ lamella at the lower left of Figure S4b, the γ phase at the left side of the interface is whiter and cleaner than that at the right side, which indicates the whiter part is a recrystallized γ phase and grows up towards the darker one. This result exactly verifies the conclusion that some γ phases increased after annealing revealed by the XRD patterns. Figure S4c shows the morphology of typical α_2/γ lamellar structures, it can be observed that the interface between α_2 and γ lamellae is very straight and there is also a growth ledge left at a α_2 lamella. The inset is the SADP captured at the interface of α_2 and γ lamellae. After indexing them, it's found that the two lamellae satisfy the Blackburn orientation relationship: $(0002)\alpha_2 // (\bar{1}1\bar{1})\gamma, [1\bar{2}10]\alpha_2 // [011]\gamma$. In addition, there is a tiny α_2 lamella which has not yet grown up in a coarse γ lamella, it seems like the tiny α_2 lamella was generated on an interface originally existing in the as-cast microstructures. Considering the distinguishable decomposition traces including inhomogeneous contrast and some residual dislocations, it can be inferred that the interface was derived from a B2/γ interface in the as-cast alloy. Consequently, the transformation process of B2/γ lamellar structures during annealing at 1250 ℃ can also be revealed on basis of the above analysis. Figure S4d shows two pieces of γ phase in blocky B2 phase. The two pieces of γ phase contain some dislocations, which indicate that these γ phases were retained from the as-cast alloy rather than generated by re-nucleation and growth. Due to there being dissolution process of γ phase during annealing as indicated by XRD analysis, it's reasonable to regard the two γ pieces as undissolved ones after annealing at 1250 ℃ for 1 hour.

In summary, when the as-cast alloy was annealed at 1250 ℃, the B2 lamellae started to decompose, instead the α_2 lamellae started to form preferentially at the γ/γ or original B2/γ interfaces due to the favorable nucleation and growth conditions. Then the two kinds of lamellar

structures gradually transformed into conventional α_2/γ ones with the annealing time increasing. Meanwhile the long rod-like γ phase in ILC area began to dissolve in blocky B2 phase partially and its spherodization occurred. With the γ phase dissolved continuously, some granular α_2 began to nucleate and grow up adjacent to blocky γ phase in the ILC area. Under the integrated effect of the decomposition of B2 lamellae in LC area and the growth of blocky B2 phase in ILC area, the content of B2 phase decreased firstly and then increased with the annealing time increasing.

Analysis about the precipitation process of nanoparticles

Three shapes of nanoparticles can be carefully distinguished as rod-like, triangular and granular, respectively (Figure 2a). Both the rod-like and triangular particles are transition phases of the granular ones, and their shape evolution sequence is as follows: rod-like → triangular → granular.[2] Based on the diffraction pattern as shown in Figure 2b, the lattice parameters corresponding to the main and secondary diffraction spots can be figured out as a=0.175 nm, c=0.259 nm and a=0.592 nm, c=0.917 nm, respectively. Comparing these lattice parameters with those of α_2 phase (a=0.578 nm, c=0.464 in PDF card), it's discovered that the lattice parameters corresponding to the secondary diffraction spots are closer to those of α_2 phase, consequently, the transition phase revealed by the secondary diffraction spots can be expressed as α', while the other transition phase can be expressed as α'' correspondingly. Furthermore, Based on the shape evolution sequence of the precipitates, it's inferred that the shape of the α'', α' and α precipitates are rod-like, triangular and granular, respectively. By reference to the classical aging precipitation process of Al-4.5 wt.% Cu alloy,[3] the precipitation process of the α nanoparticles in this research is proposed as follows: G. P. area → α'' → α' → α.

Just as the nucleation process of solidification, precipitates almost nucleate heterogeneously from solid matrix, and non-equilibrium defects such as vacancy, dislocation, grain boundary and so on can improve the free energy of material and provide appropriate nucleation sites.[2] Here it was the generated high-density short dislocations during annealing that provided substantial effective heterogeneous nucleation sites for the nanoparticles.

The short dislocations facilitated the nucleation of nanoparticles mainly from the following two aspects. On one hand, the dislocations made solute atoms segregate around dislocation cores, which provided a composition fluctuation for the nucleation of nanoparticles. In order to reduce the elastic strain energy of dislocations, large atoms such as Ti, Nb and Cr as well as interstitial atoms including O, N tended to segregate under the slip plane {111} of dislocations to offset the tensile stress, while the Al atoms tended to segregate above the slip plane instead. As a consequence, the enrichment of Ti and other elements including Cr and O under the slip plane of dislocations made the G. P. area generated on the {111} crystal plane of γ phase matrix. The G. P. areas might have a similar shape to the short dislocations, and keep a coherent relationship with the matrix to reduce the interfacial energy. On the other hand, the dislocations could promote the nucleation and growth of nanoparticles by reducing the total strain energy of crystal embryo, because relative lower strain energy can decrease the activation energy barrier for the nucleation of crystal embryo. The effect mechanism of dislocation on the total strain energy of crystal embryo is also derived from the contrary strain filed between the two sides of slip plane. Therefore, in order to obtain relative lower misfit strain energy, the coherent crystal embryo with a minus misfit (whose specific volume is less than that of the matrix) tends to nucleate in the compressive strain area which is above the slip plane of edge dislocation, while that with a positive misfit tends to nucleate under the slip plane. Both the α phase and transition phase α'

have positive misfits with the γ matrix, then the two precipitates are able to grow up more easily under the slip plane, where the composition condition also benefited the nucleation of α phase as stated above. In contrast, the α'' transition phase has a minus misfit with the γ phase matrix, which means that the α'' phase is favorable to form and grow up above the slip plane of dislocations.

As mentioned above, the G. P. areas were generated under the slip plane of dislocations. With the annealing time increasing, the G. P. areas grew up continuously and then transformed into α'' phase. Due to the minus misfit of α'' phase with the γ phase matrix, the α'' phase tended to grow upwards and thereby entered into the dislocation core area. Considering the dislocation core can provide an advantageous atomic diffusion channel for the growth of new phase, the α'' phase grew up rapidly and then transformed into the α' phase. According to Figure 2a, the length and width (or diameter) of the rod-like α'' precipitates are measured as 31.94±5.06 nm and 4.80±1.27 nm, respectively. The α'' precipitates have an approximate shape or size of the short dislocations in Figure 2f, which also verified the fact that the α'' precipitates grew up at the dislocation cores. Subsequently, since the α' phase can grow up more easily under the slip plane of dislocations, it would grow towards the underneath of the slip plane, which resulted in the triangular shape of the α' phase. With the annealing time increasing, the α' phase would develop into granular α phase in the end.

In the past years, a lot of researches on the γ → α transformation in γ-TiAl-based alloys have been conducted particularly.[4-7] It was also discovered that α phase precipitated in the interior of γ grains when single or near γ microstructures were heat-treated in the α or (α+γ) phase fields. However, what is much different from this research is that almost all of those α phases precipitated as lathes. These α lathes were found to nucleate at generated Shockley partial

dislocations and keep the Blackburn orientation relationship with the γ phase matrix, namely $\{111\}_{\gamma}//\{0001\}_{\alpha}, <110>_{\gamma} // <11\bar{2}0>_{\alpha}$. In this research, the nanoparticles were also found to nucleate at the Shockley partial dislocations sometimes, so they might also keep the above orientation relationship with the γ phase matrix, but there was no crystallographic orientation relationship observed between the nanoparticles and γ phase matrix in practice. It is probable that the precipitates started to lose the coherent relationship with γ phase matrix when they transformed into the α'' phase from the G. P. area due to the serious lattice misfit. Considering the complexity with respect to the nanoparticles precipitation process, more specific researches are required to be performed in the future.

In conclusion, why so many α nanoparticles precipitated in the γ phase matrix in sample S1 is induced by the following two reasons. On one hand, both appropriate annealing temperature and time are necessary for the formation of substantial α nanoparticles. According to the elaborated Al-Cr-Ti ternary phase diagram at 1250 ℃ by Witusiewicz et al.[8], the equilibrium phase region for the equivalent composition of Ti-44.75Al-4Cr is (α+γ) two phases region, where the α phase occupies the majority, which indicates that the formation Gibbs free energy of α is less than that of γ phase here. Therefore, the reduction in the formation Gibbs free energy provided a driving force for the precipitation of α nanoparticles from the γ phase matrix at 1250 ℃. However, with the annealing time increasing, the nanoparticles would have an obvious Ostwald ripening process. Additionally, most of the γ phase matrix would also transform into α phase at this temperature. Consequently, the two processes would lead to the coarsening and disappearance of these α nanoparticles. It's concluded that both appropriate annealing temperature and time are extremely significant for the precipitation of substantial α nanoparticles. On the other hand, high-density short dislocations generated during annealing provided substantial heterogeneous nucleation sites

for the precipitation of substantial α nanoparticles. In fact, the above two reasons are uniform and closely related, because with the annealing temperature and time increasing, the substantial short dislocations will gradually dissociated and disappeared.

Thermodynamic analysis about nucleation process of deformation twins

Deformation twinning is a uniform shear process of multiple atomic layers with the same crystal plane indices. The crystal plane where the twinning shear proceeds is called twining plane, while the direction of the uniform shear is called twinning direction. The uniform shear process of deformation twinning is carried out by the glide of Shockley partial dislocations, which makes each atomic plane (parallel to the twinning plane) of deformation twin take a certain displacement (the moduli of Shockley partial dislocation) along the twining direction against its adjacent one.[9]

The formation of deformation twin is generally considered as experiencing two stages, namely nucleation and growth, just like most first order phase transformation.[10] The nucleation process can also be classified into two categories: homogeneous and heterogeneous nucleation, in which the heterogeneous one is easier to occur in energetics. Deformation twins often heterogeneously nucleates at lattice defects, including dislocations, stacking faults, grain boundaries and so on,[10,11] because lattice defects can provide necessary stress, energy and structure conditions for the nucleation of deformation twins. In detail, the stress concentration around the lattice defects provides a driving force for the nucleation of twins.[10,12] The high included lattice strain energy of defects facilitates twin embryos to overcome the nucleation energy barrier. In addition, lattice defects can provide a structure foundation necessary for twinning glide, namely Shockley partial dislocations, directly or indirectly.

How does the deformation twinning come into being particularly? Three general categories of twinning mechanisms have been proposed so far: the pole mechanism (Cottrell and Bilby 1951),[13] the double-cross-slip mechanism (Pirouz 1987)[14] and the stimulated slip mechanism (Q. Yu and Z. Shan 2010).[15] Both the former two mechanisms involve the dissociation of dislocations. In the pole mechanism, it's the component Burgers vector of pole dislocation normal to the twinning plane that moves the twinning partial dislocation from plane to plane, by which the growth of deformation twin is realized. With respect to the double-cross-slip mechanism, the twin thickening is achieved by dislocation cross-slip.[9] In the stimulated slip mechanism, it's recognized that the stimulated slip from plane to plane is catalyzed by promoter defects, which could be screw pole dislocations, grain boundaries and surfaces. The promoter defects interact with a gliding twinning dislocation, and subsequently "infect" an atomically adjacent plane to start slipping by the same twinning dislocation Burgers vector.[16] Although there are significant differences between the three twinning mechanisms, where the inter-planar infections in the same way of twining glide are all correlated with lattice defects.

In our research (as shown in Figure S6), on one hand, whether for the as-cast Ti-45.5Al-4Cr-2.5Nb alloy or the as-annealed one, the twin density in lamellar γ phase was higher than that in massive γ phase, while the twin width had an opposite situation. These results indicate that the deformation twins are more easily generated in lamellar γ phase than in the massive one, which has also been concluded in other relevant researches.[17,18] It's generally believed that the lamellar interfaces, which can provide effective heterogeneous nucleation sites for deformation twinning, result in the above-state phenomenon. On the other hand, the deformation twins are more easily generated in the as-annealed Ti-45.5Al-4Cr-2.5Nb alloys than in the as-cast alloy (Figure 4 and S6). As shown in Figure 2, there were substantial Shockley partial dislocations and stacking

faults generated after the as-cast alloy annealed, these dislocations and stacking faults are supposed to the main reason for the generation of high-density deformation nanotwins in as-annealed alloys. In order to more deeply understand the exact reasons for the two above phenomena, the nucleation process of deformation twins in massive and lamellar γ phase will be analyzed particularly in the view of thermodynamics as follows.

For more extensive representativeness, we will research two nucleation situations of deformation twins, namely inside massive γ phase and at α_2/γ interface accompanied by growing across the γ lamella, respectively. In each nucleation situation, both homogeneous and heterogeneous (nucleation on a stacking fault) modes will be discussed. Based on the comprehensive considerations of simplification of calculation and consistency to reality, it's assumed that deformation-twin embryo is in the shape of cuboid or monoclinic hexahedron with respect to different nucleation situations, and the basal plane of the embryo is square with the size of $l \times l$ (as shown in Figure S7). In the process of twinning dislocation glide, both the resistance from dislocation forests and the interaction between dislocations will be neglected.

Prior to thermodynamic analysis on the nucleation process of deformation twins, it's necessary to know about the stress condition of twinning dislocations when they are gliding. The driving force for the glide of twining dislocation is the applied shear stress $\boldsymbol{\tau}$, while the resistance to the dislocation glide is much different between the first and the subsequent twinning planes. On the first twinning plane, the twinning dislocation inevitably suffers the lattice resistance firstly when gliding, it's assumed that the lattice resistance to the glide of twining dislocation is approximately equal to the Peierls-Nabarro stress $\boldsymbol{\tau_{P\text{-}N}}$ here. In addition, due to the first glide producing an intrinsic stacking fault, the twinning dislocation also suffers a resistance from the interface tension of stacking fault when gliding. This resistance is equal to γ/b, where γ and b are

the stacking fault energy of γ-TiAl phase and the moduli of Burgers vector of twinning dislocation, respectively. On the subsequent twinning planes, because of the glide of twinning dislocation no longer producing new stacking faults, the twinning dislocation only suffer the lattice resistance when gliding. In conclusion, the resultant tress acting on the twinning dislocation Σf when gliding can be expressed as,

$$\sum f = \begin{cases} \tau - \tau_{P-N} - \dfrac{\gamma}{b}, N = 1 \\ \tau - \tau_{P-N}, N \geq 2, N \in Z \end{cases} \tag{S1}$$

Where the N is the sequence number of twinning planes, and the Peierls-Nabarro stress $\tau_{P\text{-}N}$ can be obtained by the following equation[19]

$$\tau_{P-N} = \frac{2G}{1-\upsilon} \exp\left[-\frac{2\pi\delta}{(1-\upsilon)b} \right] \tag{S2}$$

In which the G and v are the shear modulus and Poisson's ratio of γ-TiAl phase, respectively. Consequently, only when it's $\Sigma f \geq 0$ can the twinning dislocation glide. Next, the nucleation process of deformation twins in γ-TiAl phase will be analyzed specifically in the following two situations.

(1) Nucleation inside massive γ phase (which is called the first situation here)

At first, the homogeneous nucleation process of deformation twins will be discussed. When the applied shear stress $\boldsymbol{\tau}$ is high enough to make the $\Sigma f \geq 0$, the twinning dislocation will glide to make the deformation-twin embryo generated (Figure S7a). The main activation energy barrier for the nucleation of deformation twins is the increase of interfacial energy, while the constrained strain energy of the twin embryo is negligible on the assumption of the applied stress not exceeding the yield stress.[10] Consequently, the variation of Gibbs free energy ΔG_{hom} mainly consists of three parts for the generation of deformation-twin embryo. The first one is the

reduction of free energy derived from the work done by the applied shear stress $\boldsymbol{\tau}$, which is expressed as $-W$; the second one is the increase of free energy induced by the area expanding of coherent twin boundary (or stacking fault), which is expressed as A_γ; the last one is the increase of free energy induced by the area expanding of incoherent twin boundary, which is expressed as A_σ. Namely

$$\Delta G_{hom} = -W + A_\gamma + A_\sigma \tag{S3}$$

Where the W is equal to the total work done by the applied shear stress $\boldsymbol{\tau}$ to each twinning atomic plane of the embryo, therefore the W can be expressed as

$$W = \sum_{i=1}^{n} i\tau bl^2 = \frac{1}{2}\left(n^2 + n\right)\tau bl^2 \tag{S4}$$

According to the established model of the deformation-twin embryo (see Figure S7a), the increased area of stacking fault is l^2, while the increased area of incoherent twin boundaries is $4hl$. Also because $h=n\delta$, the eq (S3) can be expressed specifically as follows,

$$\Delta G_{hom} = -\frac{1}{2}\left(n^2 + n\right)\tau bl^2 + \gamma l^2 + 4n\delta l\sigma \tag{S5}$$

In which, the σ is the interfacial energy of incoherent twin boundary of γ-TiAl phase. Based on the eq (S5), the critical size of deformation-twin nucleus can be obtained by establishing and solving the following equation set,

$$\begin{cases} \dfrac{\partial \Delta G_{hom}}{\partial l} = 0 \\ \dfrac{\partial \Delta G_{hom}}{\partial n} = 0 \end{cases} \tag{S6}$$

Then the critical size of the deformation twin nucleus (the critical size parameters are marked by asterisks) can be solved as,

$$\begin{cases} n^* = \dfrac{4\gamma}{\tau b} \\ l^* = \dfrac{8\sigma\delta}{8\gamma + \tau b} \end{cases} \tag{S7}$$

Substitute the solved expressions of n^* and l^* into eq (S5), the nucleation energy barrier for the homogeneous deformation twins can be calculated as,

$$\Delta G_{hom}{}^{*} = \frac{64\sigma^2\delta^2\gamma}{\tau b\left(8\gamma + \tau b\right)} \tag{S8}$$

In accordance to existing researches,[19] there is a certain proportional relationship between the stacking fault energy and the incoherent twin boundary energy in crystal materials, the latter is approximately 2.5-fold of the former. Therefore, it can be known from eqs (S7) and (S8) that both the critical size parameters (n^* and l^*) and nucleation energy barrier of deformation-twin nucleus are in direct proportion to the stacking fault energy of γ-TiAl phase, but in inverse proportion to the applied shear stress. Consequently, on one hand, every method available to reduce the stacking fault energy of γ-TiAl phase can improve the deformation-twin forming ability of γ-TiAl phase; on the other hand, local stress concentration is also beneficial to the nucleation of deformation twins on the condition that the applied macro-stress is definite.

By reference to existing literatures,[20,21] the values of involved parameters in eqs (S7) and (S8) can be acquired directly or by further calculation, substitute these values into the equations, the concrete values of the critical size of homogeneous deformation-twin nucleus and the corresponding nucleation energy barrier can be calculated out, respectively. The necessary parameters used for calculation are presented in Table S4. According to the results obtained from the stress analysis to twinning dislocation on gliding, it's indicated that the condition of $\tau \geq \tau_{P\text{-}N} + \gamma/b$ must be satisfied when stacking faults are created or expand in the process of deformation twinning. For the sake of acquiring both the critical size of deformation-twin nucleus and the

nucleation energy barrier, the τ value in eqs (S7) and (S8) should adopt the critical value for the glide of twinning dislocation correspondingly, namely $\tau = \tau_{P\text{-}N} + \gamma/b$ =396.36MPa here. After all the involved parameters in eqs (S7) and (S8) known, the critical size of homogeneous deformation-twin nucleus and corresponding nucleation energy barrier can be calculated as n^*=4, l^*=0.513nm; $\Delta G_{hom}{}^* = 1.51\times10^{-19}$J.

Based on the above discussion about homogeneous nucleation process of deformation twins, the heterogeneous nucleation mode will also be discussed. Considering the close relationship between twinning and stacking fault, it's assumed that deformation twins nucleate heterogeneously on a stacking fault in this research. As shown in Figure S7c, it's assumed that the stacking fault is intrinsic and in square with the size of $l_0\times l_0$.

When $0<l_0<l$, namely the glide of twinning dislocation is required to expand the stacking fault in the process of deformation-twin nucleation, the condition of $\tau \geq \tau_{P\text{-}N} + \gamma/b$ need be satisfied. As a consequence, the variation of Gibbs free energy ΔG_{het} in the heterogeneous nucleation process is also composed of three parts similar to that in the homogeneous nucleation process, and can be expressed in detail as follows,

$$\begin{aligned}\Delta G_{het} &= -W + A_\gamma + A_\sigma \\ &= -\left[\tau b\left(l^2 - l_0^2\right) + \frac{1}{2}\tau b l^2\left(n+2\right)\left(n-1\right)\right] + \gamma\left(l^2 - l_0^2\right) + 4\delta\sigma\left(nl - l_0\right) \\ &= -\frac{1}{2}\left(n^2+n\right)\tau b l^2 + \gamma l^2 + 4n\delta l\sigma + \left(\tau b - \gamma\right)l_0^2 - 4\delta\sigma l_0\end{aligned} \quad \text{(S9)}$$

Compared eq (S9) with eq (S5), it's found that both are the same except two more constant terms in eq (S9). Thus, the critical size of the heterogeneous deformation-twin nucleus is identical to that for the homogeneous nucleation. Moreover, the nucleation energy barrier for the

heterogeneous deformation twins ΔG_{het}^{*} can be achieved by combination with the eq (S8), namely

$$\Delta G_{het}^{*}=\frac{64\sigma^{2}\delta^{2}\gamma}{\tau b\left(8\gamma+\tau b\right)}+\left(\tau b-\gamma\right)l_{0}^{2}-4\delta\sigma l_{0} \tag{S10}$$

Make $f\left(l_{0}\right)=\left(\tau b-\gamma\right)l_{0}^{2}-4\delta\sigma l_{0}$, then it's easy to known that the $f(l_0)<0$ when $0<l_0<l^*$, and the $f(l_0)$ infinitely tends to its minimum with the l_0 approaching to l^* (when $l_0=l^*$, the $\Delta G_{het}^{*}=7.52\times10^{-20}J$). Consequently, the ΔG_{het}^{*} is always less than $\Delta G_{hom}{}^{*}$ and decreases continuously with the increase of l_0. It's indicated that deformation twins are easier to nucleate heterogeneously on a stacking fault ($l_0<l^*$) than to nucleate homogeneously.

When $l_0\geq l$, it means that the glide of twinning dislocation isn't required to expand the stacking fault in the process of deformation-twin nucleation. Therefore, the variation of Gibbs free energy ΔG_{het} in the heterogeneous nucleation process is composed of two parts, and can be expressed specifically as follows,

$$\begin{aligned}\Delta G_{het}&=-W+A_{\sigma}\\&=-\frac{1}{2}\left(n^{2}+n\right)\tau bl^{2}+4n\delta l\sigma\end{aligned} \tag{S11}$$

Where the n is the number of twinning atomic plane(s) of deformation-twin embryo excluding the one on which the heterogeneous stacking fault exists, and $n\geqslant1$. If the n is assumed as a constant value, then the ΔG_{het} is a quadratic function of l, and both the critical size of the heterogeneous deformation-twin nucleus and the nucleation energy barrier for the heterogeneous deformation twins can be calculated as follows,

$$l^{*}=\frac{4\delta\sigma}{\left(n+1\right)\tau b} \tag{S12}$$

$$\Delta G_{het}^{*} = \frac{8\delta^2\sigma^2 n}{(n+1)\tau b} \tag{S13}$$

As shown in eqs (S12) and (S13), both the l^* and ΔG_{het}^{*} are the functions of n. It's easy to know that the l^* monotonously decreases with the n increasing, while the ΔG_{het}^{*} has an inverse variation trend. Therefore, when n=1, the ΔG_{het}^{*} has the minimum of 8.50×10^{-20}J. Although the critical applied shear stress to drive the motion of twinning dislocation is as low as $\tau_{P\text{-}N}$ when $l_0 \geq l$, in order to be compared with the homogeneous nucleation mode better, the values of n and τ in both eqs (S12) and (S13) are similarly adopted as 3 and 396.36MPa ($\tau_{P\text{-}N} + \gamma/b$), respectively. When n=3, the l^*=0.576nm and the $\Delta G_{het}^{*} = 1.28\times10^{-19} J$. By comparing these data with the corresponding critical values for the homogeneous nucleation of deformation-twin embryo, it's revealed that to nucleate a deformation-twin embryo with a similar size, it's more favorable in the heterogeneous nucleation mode, on a large enough stacking fault ($l_0 \geq l$), than in the homogeneous nucleation mode.

In conclusion, when deformation twins nucleate inside massive γ phase, in heterogeneous nucleation mode is easier than in homogeneous one.

(2) Deformation twins initiating at the α_2/γ interface and growing across the γ lamella (which is called the second situation)

When a deformation twin nucleates at the α_2/γ interface and grows across the γ lamella, actually this situation is in a kind of heterogeneous nucleation mode where the nucleation site is the α_2/γ interface, as illustrated in Figure S7b. In order to research the effect of stacking fault on the nucleation process of deformation twin in this situation, two conditions that there is no and a pre-existing stacking fault with the size of $l_0 \times l_0$ on the twinning plane of γ lamella will be

discussed. For the convenience of description and comparison, the two conditions are also called as homogeneous and heterogeneous nucleation, respectively, corresponding to the first situation.

At first, the homogeneous nucleation mode will be analyzed. As shown in Figure S7b, the variation of Gibbs free energy ΔG_{hom} in this situation also consists of three parts, which are analogous to those in the first situation. The unique difference is the third term between the two ΔG_{hom} expressions, and is mainly derived from two aspects, namely the difference in the shape of deformation-twin embryo between two situations and the beneficial effect of the α_2/γ interface on the formation of incoherent twin boundary in this situation. For simplifying the calculation process, it's assumed that the α_2/γ interfacial energy is equal to that of the incoherent twin boundary and keeps constant in the process of deformation twinning. Therefore the ΔG_{hom} in this situation can be expressed specifically as follows,

$$\begin{aligned} \Delta G_{hom} &= -W + A_\gamma + A_\sigma \\ &= -\frac{1}{2}\left(n^2 + n\right)\tau b l^2 + \gamma l^2 + 3.06 n\delta l\sigma \end{aligned} \tag{S14}$$

By establishing the equation set (S6) of eq (S14) similar to the first situation, the critical size of homogeneous deformation-twin nucleus in this situation can be solved. Substitute the obtained critical size of homogeneous deformation-twin nucleus into the eq (S14), the nucleation energy barrier for homogeneous deformation twins in this situation can also be solved. Their expressions are as follows,

$$\begin{cases} n^* = \dfrac{4\gamma}{\tau b} \\ l^* = \dfrac{6.12\sigma\delta}{8\gamma + \tau b} \\ \Delta G_{hom}{}^* = \dfrac{37.45\sigma^2\delta^2\gamma}{\tau b\left(8\gamma + \tau b\right)} \end{cases} \tag{S15}$$

By comparing the eq (S15) with the eqs (S7) and (S8), it's found that the critical volume of the homogeneous deformation-twin nucleus in this situation is about 58.52% of that in the first situation when the applied shear stress τ is the same, which makes the corresponding nucleation energy barrier in this situation have the same percentage of that in the first situation. Substitute the values of involved parameters into eq (S15), the nucleation energy barrier for the homogeneous deformation-twin nucleation in this situation can be calculated as 8.84×10^{-20}J.

With respect to the heterogeneous nucleation mode, namely deformation twins nucleate on a stacking fault, the variations of Gibbs free energy ΔG_{het} in this process are also similar to that in the first situation whether when $0<l_0<l$ or $l_0\geq l$. The expressions of ΔG_{het} in this situation have the same constituent terms with those in the first situation correspondingly except the coefficient of the A_σ terms (being 3.06 in this situation). Therefore both the critical size of heterogeneous deformation-twin nucleus and the corresponding nucleation energy barrier can also be calculated in the same ways with respect to the first situation. It can be also concluded that deformation twins are easier to nucleate on a stacking fault (heterogeneously) than nucleate homogeneously in a lamellar γ phase by a series of comparisons. In addition, it's found that all the corresponding ΔG_{het}^{*} values in this situation are approximately 58.5% of those in the first situation. Relative details for this situation are as follows, when $0<l_0<l$, the ΔG_{het}^{*} value is approaching to 4.41×10^{-20}J with the l_0 approaching to l^*; when $l_0\geq l$, the minimum of ΔG_{het}^{*} is 4.97×10^{-20}J with the value of n=1, as well as when n=3, the ΔG_{het}^{*} value is 7.46×10^{-20}J correspondingly.

In conclusion, whether in homogeneous or heterogeneous nucleation mode, the nucleation energy barrier for deformation twins generated in lamellar γ phase is only 58.5% of that for deformation twins generated in massive γ phase, namely deformation twins are easier to be generated in the lamellar γ phase than in the massive one. Based on the above analysis, the

beneficial effect of lamellar boundary to the generation of deformation twins can be inferred further. It has been assumed above that the α_2/γ interfacial energy is equal to that of the incoherent twin boundary and keeps constant in the process deformation twinning. Actually, it's probable that the α_2/γ boundary is in a high-energy state and its interfacial energy is higher than that of the incoherent twin boundary in γ phase. Therefore, it's also probable that the energy of the α_2/γ interface is reduced in the process of deformation twinning, which can make the nucleation energy barrier for deformation twins less. As a consequence, a high-energy α_2/γ interface is probably beneficial to the nucleation of deformation twins.

It's well known that deformation twinning is closely connected with the twinning dislocation, and a short twinning dislocation can be regarded as an effective nucleation site for deformation twins. Based on this viewpoint, the nucleation rate expression of deformation twins can be constructed similarly by referring to the nucleation rate expressions of dislocations or solid phase nucleating from liquid or other solid phases.[2,22,23] On the condition that both the applied shear stress and temperature are definite, it's assumed that C is the equivalent number of deformation-twin nucleation sites per unit volume of γ phase, then the number of critical deformation-twin nucleus per unit volume of γ phase C^* can be expressed as,

$$C^* = C\exp\left(-\frac{\Delta G^*}{kT}\right) \tag{S16}$$

Where the k is the Boltzmann constant, the T is the absolute temperature, the ΔG^* is the nucleation energy barrier for deformation twins. Define f is the attempt frequency of critical deformation-twin nucleus turning into stable deformation twins, then the deformation-twin nucleation rate R can be expressed as follows,

$$R=fC\exp\left(-\frac{\Delta G^*}{kT}\right) \tag{S17}$$

It's worth noting that the eq (S17) is a general expression for deformation-twin nucleation on different conditions, including homogeneous and heterogeneous nucleation in different morphologies of γ phase, as well as the f, C and ΔG^* correspond to different values with the applied conditions changed. Combined relevant ΔG^* expressions with the eq (S17), it's found that the deformation-twin nucleation rate R improves significantly with the increase of applied shear stress τ, then the dependency curves of R on τ can be schematically plotted as steeply increased ones just as shown in Figure S8c and d. By a graphic method as illustrated in Figure S8, it can be concluded that whether nucleation in heterogeneous or homogeneous mode, as well as nucleation in lamellar or in massive γ phase, on one hand, the critical applied shear stress for γ phase deformation-twin nucleation to the former is lower than that to the latter with the same of the other conditions; on the other hand, the deformation-twin nucleation rate for the former is much higher than that for the latter with the applied shear stress definite. These conclusions exactly and clearly illuminates why high density deformation nanotwins were generated in the as-annealed TiAl alloys, especially in the lamellar γ phase, rather than in the as-cast TiAl alloy (as shown in Figure S6e and f).

Statistics about the compressive property of existing γ-TiAl-based alloys

The references used for the statistics about the compressive property of existing γ-TiAl-based alloys are included in ref. (*24*) to (*36*).

References

(1) Nie, G.; Ding, H.; Chen, R.; etc. Microstructural control and mechanical properties of Ti-47Al-2Cr-2Nb alloy by directional solidification electromagnetic cold crucible technique. *Mater. Des.* **2012**, *39*, 350-357.

(2) Porter, D. A.; Easterling, K. E.; Sherif, M. Y. *Phase transformations in Metals and Alloys, 3rd edition;* CRC Press: Boca Raton, 2009.

(3) Ringer, S. P.; Hono, K. Microstructural evolution and age hardening in aluminium alloys: atom probe field-ion microscopy and transmission electron microscopy studies. *Mater. Charact.* **2000**, *44*, 101-131.

(4) Ramanujan, R. V. The transformation between the γ and α phases in binary and ternary γ-based titanium aluminides. *Acta Metall. Mater*. **1994**, *42*, 2313-2322.

(5) Kumagai, T.; Abe, E.; Kimura, T.; etc. The γ→α phase transformation in γ-based TiAl alloy. *Scr. Mater*. **1996**, *34*, 235-242.

(6) Zhang, W.; Chen, G. Precipitation of α phase in the massive and feathery structures in TiAl alloys during aging in the single α field. *J. Mater. Sci. Technol.* **1999**, *15*, 469-472.

(7) Li, Z.; Cao, C. γ→α precipitation transformation in γ-TiAl alloy. *Chin. J. Nonferrous Met.* **2003**, *13*, 827-834. (in Chinese)

(8) Witusiewicz, V. T.; Bondar, A. A.; Hecht, U.; etc. Thermodynamic re-modelling of the ternary Al-Cr-Ti system with refined Al-Cr description. *J. Alloys Compd.* **2015**, *644*, 939-958.

(9) Lagerlöf, K. P. D.; Castaing, J.; Pirouz, P.; etc. Nucleation and growth of deformation twins: a perspective based on the double-cross-slip mechanism of deformation twinning. *Philos. Mag. A* **2002**, *82*, 2841-2854.

(10) Christian, J. W.; Mahajan, S. Deformation twinning. *Prog. Mater. Sci.* **1995**, *39*, 1-157.

(11) Jin, Z.; Bieler, T. R. An in-situ observation of mechanical twin nucleation and propagation in TiAl. *Philos. Mag. A* **1995**, *71*, 925-947.

(12) Wang, J.; Huang, H. Shockley partial dislocations to twin: another formation mechanism and generic driving force. *Appl. Phys. Lett.* **2004**, *85*, 5983-5985.

(13) Cottrell, A. H.; Bilby, B. A. LX. A mechanism for the growth of deformation twins in crystals. *Philos. Mag. A* **1951**, *42*, 573-581.

(14) Pirouz, P. Deformation mode in silicon, slip or twinning? *Scri.Metall.* **1987**, *21*, 1463-1468.

(15) Yu, Q.; Shan, Z.; Li, J.; etc. Strong crystal size effect on deformation twinning. *Nature* **2010**, *463*, 335-338.

(16) Yu, Q.; Qi, L.; Chen, K.; etc. The nanostructured origin of deformation twinning. *Nano Lett.* **2012**, *12*, 887-892.

(17) Yoo, M. H.; Hishinuma, A. Deformation twinning in TiAl: effects of defect clustering. *Met. Mater.* **1997**, *3*, 65-74.

(18) Yoo, M. H. Dislocation mechanisms for deformation twinning in the $L1_0$ structure. *Scr. Mater.* **1998**, *39*, 569-575.

(19) Hu, G.; Cai, X.; Rong, Y. *Fundamentals of Materials Science, 2nd edition;* Shanghai Jiao Tong University Press: Shanghai, 2006. (in Chinese)

(20) Lipsitt, H. A.; Shechtman, D.; Schafrik, R. E. The deformation and fracture of TiAl at elevated temperatures. *Metall. Trans. A* **1975**, *6A*, 1991-1996.

(21) Wen, Y. F.; Sun, J. Generalized planar fault energies and mechanical twinning in gamma TiAl alloys. *Scr. Mater.* **2013**, *68*, 759-762.

(22) Bei, H.; Gao, Y. F.; Shim, S.; etc. Strength differences arising from homogeneous versus heterogeneous dislocation nucleation. *Phys. Rev. B* **2008**, *77*, 060103.

(23) Zhu, T.; Li, J.; Samanta, A.; etc. Temperature and strain-rate dependence of surface dislocation nucleation. *Phys. Rev. Lett.* **2008**, *100*, 025502.

(24) Cao, R.; Li, L.; Chen, J. H.; etc. Study on compression deformation, damage and fracture behavior of TiAl alloys: Part I. Deformation and damage behavior. *Mater. Sci. Eng. A* **2010**, *527*, 2455-2467.

(25) Li, L.; Cao, R.; Zhang, J.; etc. Study on compressive fracture behaviors of TiAl-based alloys at different strain rates. *Chin. J. Rare Metals* **2008**, *32*, 409-414. (in Chinese)

(26) Chen, J. H.; Cao, R.; Wang, G. Z.; etc. Study on notch fracture of TiAl alloys at room temperature. *Metall. Mater. Trans. A* **2004**, *35A*, 439-456.

(27) Xiao, S.; Tian, J.; Xu, L.; etc. Microstructures and mechanical properties of TiAl alloy prepared by spark plasma sintering. *Trans. Nonferrous Met. Soc. China* **2009**, *19*, 1423-1427.

(28) Bohn, R.; Klassen, T.; Bormann, R. Room temperature mechanical behavior of silicon-doped TiAl alloys with grain sizes in the nano- and submicron-range. *Acta mater.* **2001**, *49*, 299-311.

(29) Pyo, S. G.; Chang, Y. W.; Kim, N. J. Microstructure and mechanical properties of duplex TiAl alloys containing Mn. *Met. Mater.* **1995**, *1*, 107-115.

(30) Nazarova, T. I.; Imayev, V. M.; Imayev, R. M.; etc. Study of microstructure and mechanical properties of Ti-45Al-(Fe,Nb) (at. %) alloys. *Intermetallics* **2017**, *82*, 26-31.

(31) Zheng, D.; Chen, R.; Ma, T.; etc. Microstructure modification and mechanical performances enhancement of Ti44Al6Nb1Cr alloy by ultrasound treatment. *J. Alloys Compd.* **2017**, *710*, 409-417.

(32) Chen, R.; Zheng, D.; Ma, T.; etc. Effects of ultrasonic vibration on the microstructure and mechanical properties of high alloying TiAl. *Sci. Rep.* **2017**, *7*, 41463.

(33) Chen, R.; Zheng, D.; Ma, T.; etc. Effects and mechanism of ultrasonic irradiation on solidification microstructure and mechanical properties of binary TiAl alloys. *Ultrason. Sonochem.* **2017**, *38*, 120-133.

(34) Kartavykh, A.V.; Asnis, E. A.; Piskun, N. V.; etc. Microstructure and mechanical properties control of γ-TiAl (Nb, Cr, Zr) intermetallic alloy by induction float zone processing. *J. Alloys Compd.* **2015**, *643*, S182-S186.

(35) Kartavykh, A.V.; Asnis, E. A.; Piskun, N. V.; etc. A promising microstructure/deformability adjustment of β-stabilized γ-TiAl intermetallics. *Mater. Lett.* **2016**, *162*, 180-184.

(36) Wang, Y. Microstructure and Mechanical Properties of Directionally Solidified Ti-(43-48)Al-2Cr-2Nb Alloys. Ph. D. Thesis, Harbin Institute of Technology, October 2015. (in Chinese)

Figures

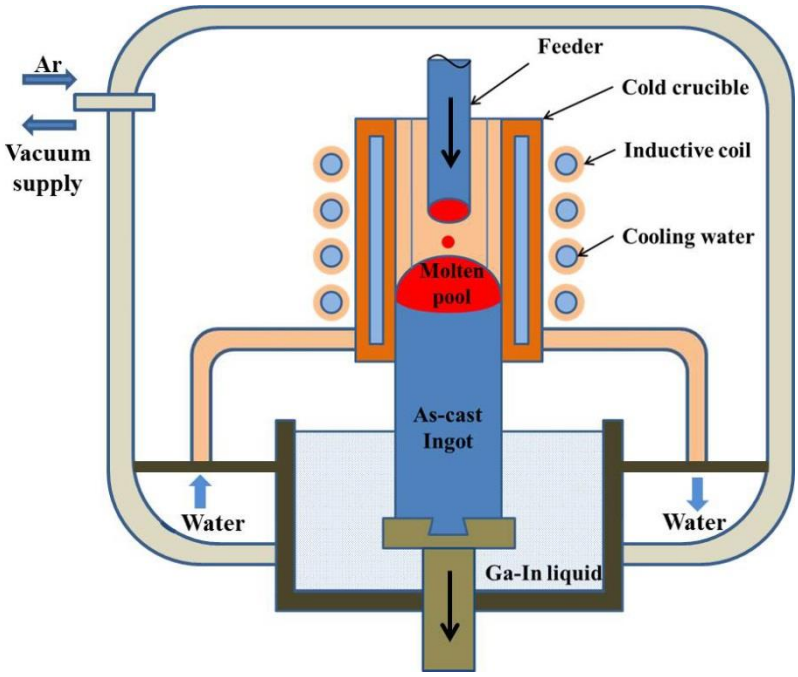

Figure S1. Schematic diagram of electromagnetic cold crucible (EMCC) multifunctional continuous casting equipment.

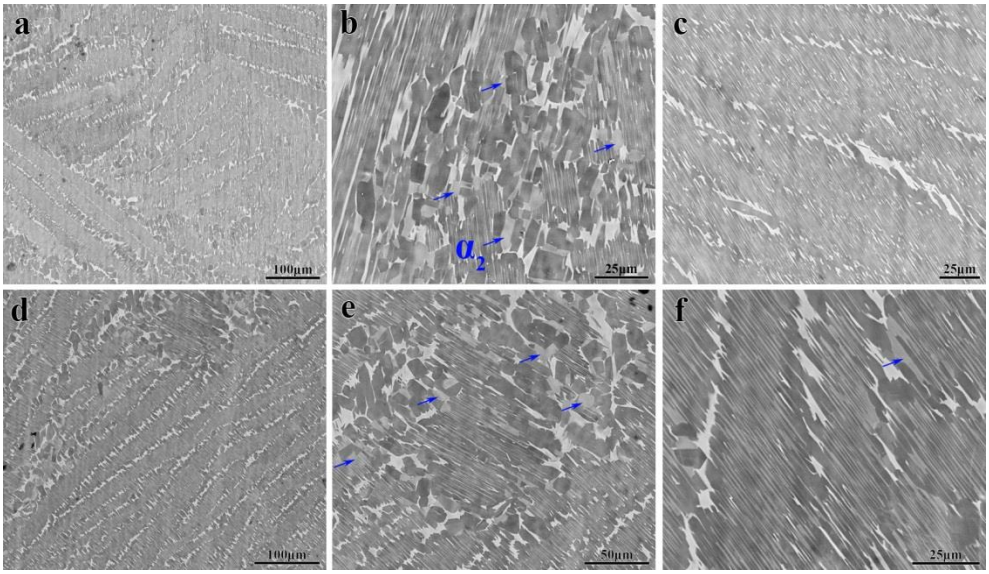

Figure S2. Microstructure of as-annealed Ti-45.5Al-4Cr-2.5Nb alloys. All images are in back-scattered electronic (BSE) mode. (a) ~ (c) are taken from sample S1 which was annealed at 1250 ℃ for 1 hour and cooled in air, in which (a) is a low magnification image, while (b) and (c) are higher magnification images obtained from inter lamellar-colonies (ILC) and lamellar colonies (LC) area, respectively; correspondingly, (d) ~ (f) are from sample S2 which was annealed at 1250 ℃ for 2 hours and cooled in air.

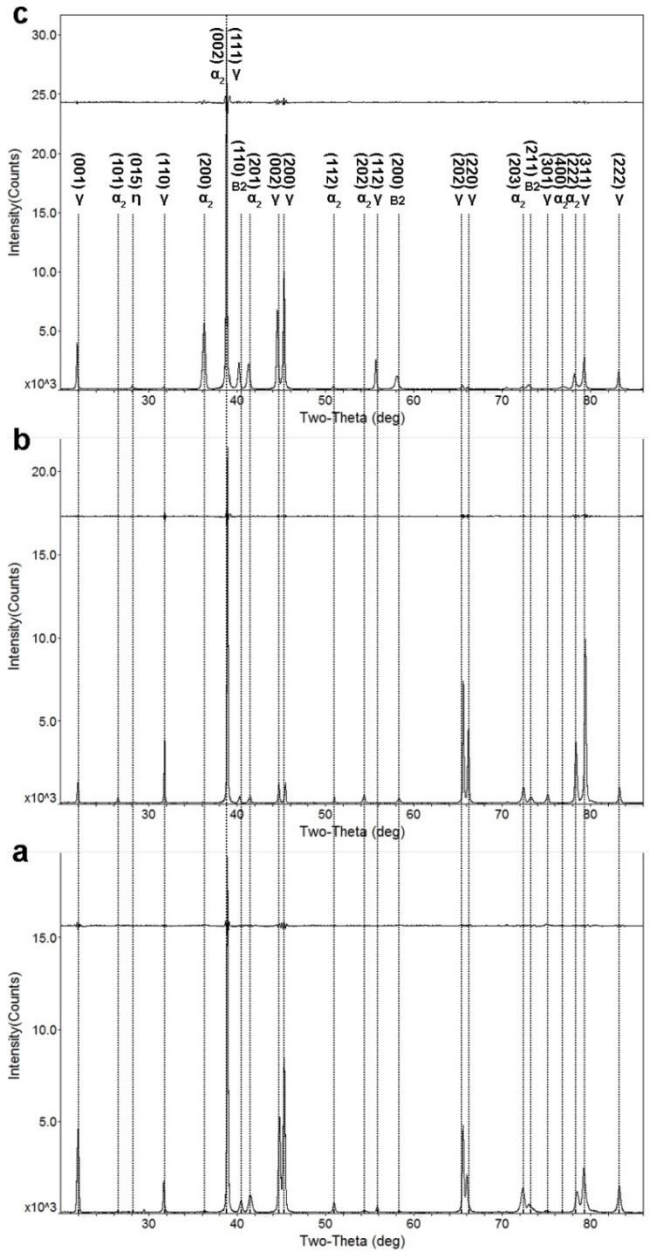

Figure S3. XRD patterns of as-cast and annealed Ti-45.5Al-4Cr-2.5Nb alloys. (a) As-cast, (b) annealed at 1250 ℃ for 1 hour, (c) annealed at 1250 ℃ for 2 hours. Major peaks have been marked according to their corresponding phase and crystal plane, symbols γ, α_2 and η represent TiAl, Ti_3Al and $TiAl_2$ phases, respectively. The solid lines above each pattern are the residual intensities between Rietveld fits and observed data, all the residual intensities are less than 10% here.

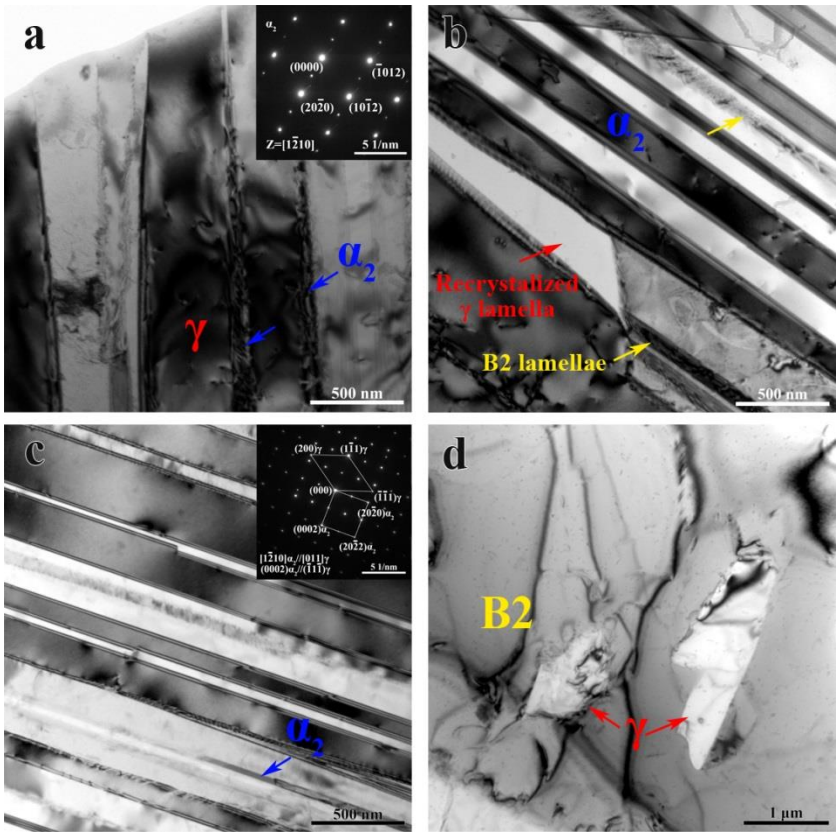

Figure S4. TEM bright-field images of as-annealed Ti-45.5Al-4Cr-2.5Nb alloy (annealed at 1250 ℃ for 1 hour). (a) Some α_2 lamellae generated between γ lamellae, the inset is the diffraction pattern of a α_2 lamella. (b) The morphology of α_2/γ lamellar structures transformed incompletely, some pieces of B2 lamellae can also be observed in the lamellar structures. (c) The morphology of typical α_2/γ lamellar structures, the inset is their diffraction patterns. (d) Two pieces of γ phase not dissolved completely in a blocky B2 phase.

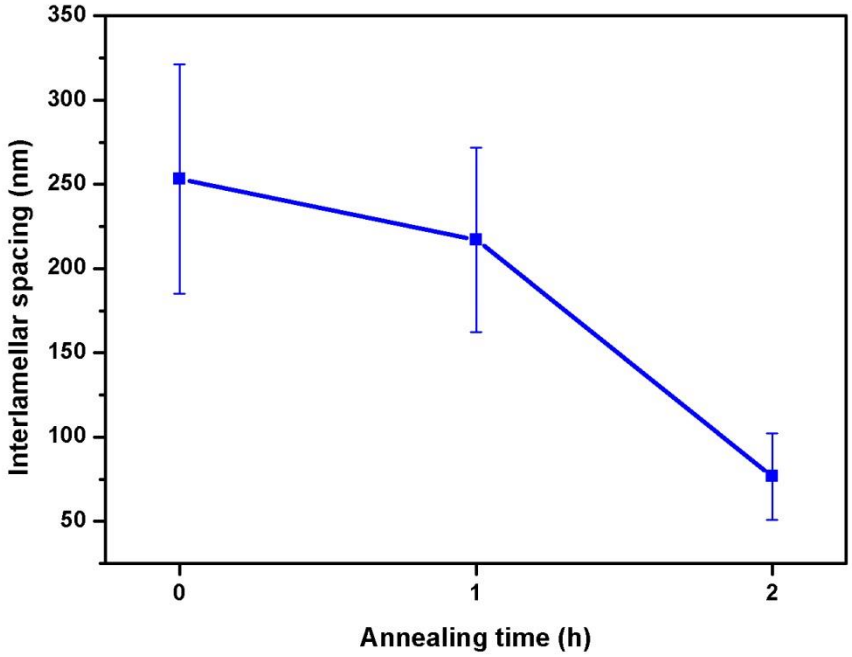

Figure S5. Dependence of the inter-lamellar spacing of Ti-45.5Al-4Cr-2.5Nb alloys on the annealing time at 1250℃. The annealing time of zero corresponds to the as-cast alloy. With the increase of annealing time, the inter-lamellar spacing decreased gradually, which is mainly due to the generation of α_2 lamellae and γ annealing twins in the annealing process. Especially, when the as-cast alloy was annealed at 1250 ℃ for 2 hours, the inter-lamellar spacing could reduce to about 77 nm. The inter-lamellar spacing indicates the average distance between lamellar interfaces here.

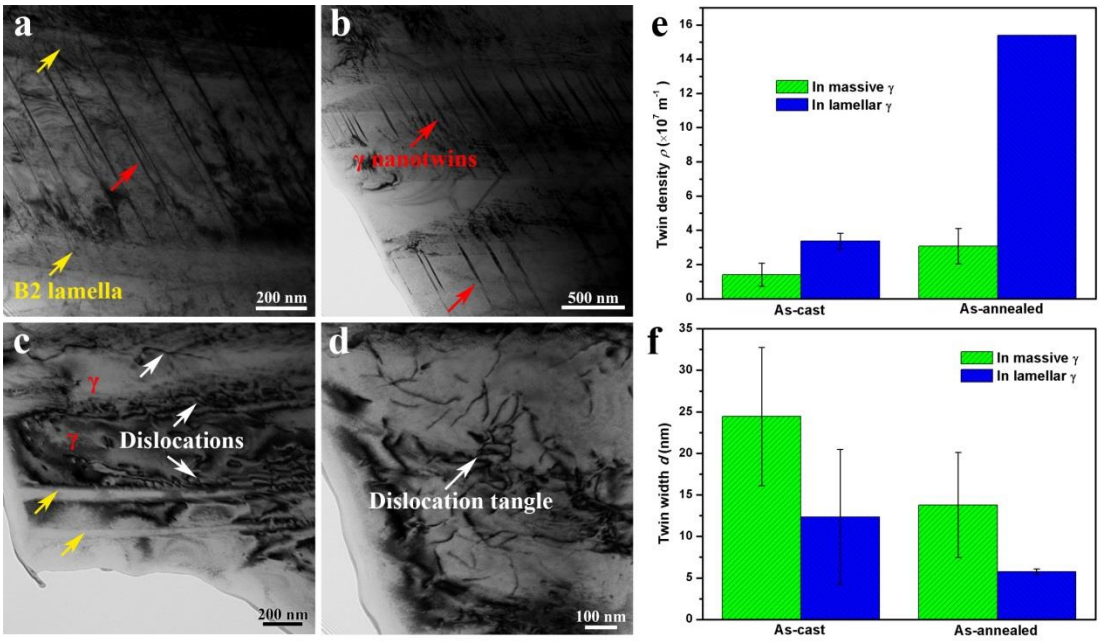

Figure S6. Deformation microstructures of as-cast Ti-45.5Al-4Cr-2.5Nb alloy after compressed to a plastic strain of 7.1% and comparison diagrams of the twin density (e) and width (f) of deformation twins in deformation microstructures between the as-cast and as-annealed alloy (annealed at 1250 ℃ for 1 hour, as shown in Figure 4). (a), (b) Bright-field TEM images shown the γ deformation nanotwins generated in lamellar and massive γ phase, respectively. (c), (d) Bright-field TEM images of dislocations generated in lamellar and massive γ phase, respectively. As shown in (c) and (d), substantial dislocations accumulated at the lamellar interfaces after deformation, meanwhile there were also lots of dislocation tangles generated in the massive γ phase.

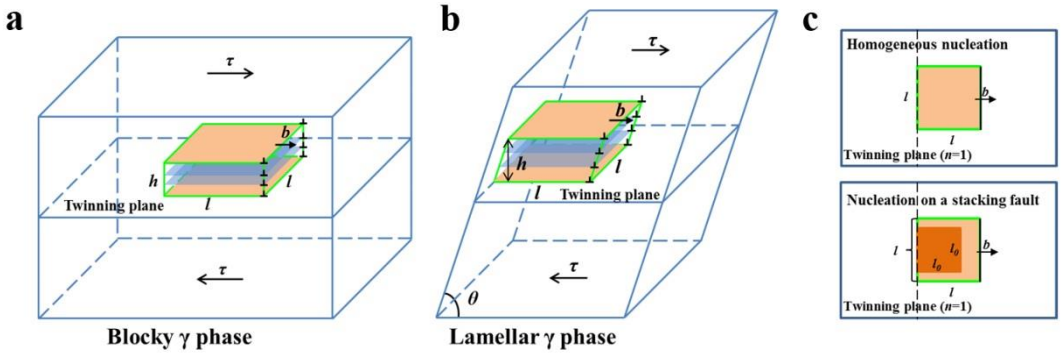

Figure S7. Schematic diagrams of the nucleation process of deformation twins in γ-TiAl phase. (a) Deformation twins nucleate in blocky γ phase. The Greek letter $\boldsymbol{\tau}$ is the shear stress applied on the γ phase unit, $\boldsymbol{b}$ is the Burgers vector of twinning dislocation, here $\boldsymbol{b}=\frac{1}{6}\left[11\bar{2}\right]$. It's assumed that the deformation-twin embryo has the size of $l\times l\times h$, here $h=n\delta$, in which the n is the number of twinning atomic plane(s) of the embryo, and δ is the inter-planar spacing of twinning plane {111}. (b) Deformation twins initiate at the α_2/γ interface and grow across the γ lamella. The θ is the intersection angle between the twinning plane and the α_2/γ interface. According to the Blackburn relationship between γ and α_2 phase in lamellar structures, the θ value can be calculated as 70.53° easily. (c) Schematic diagrams of two deformation twining conditions for the first twinning atomic plane when the deformation-twin embryo nucleates homogeneously (the upper image) and on a stacking fault (the under one), respectively. The dash lines indicate the α_2/γ interface when the deformation twins are generated in lamellar γ phase, besides the dark square with the size of $l_0\times l_0$ in the below image represents the staking fault acting as the heterogeneous nucleation site for deformation twins.

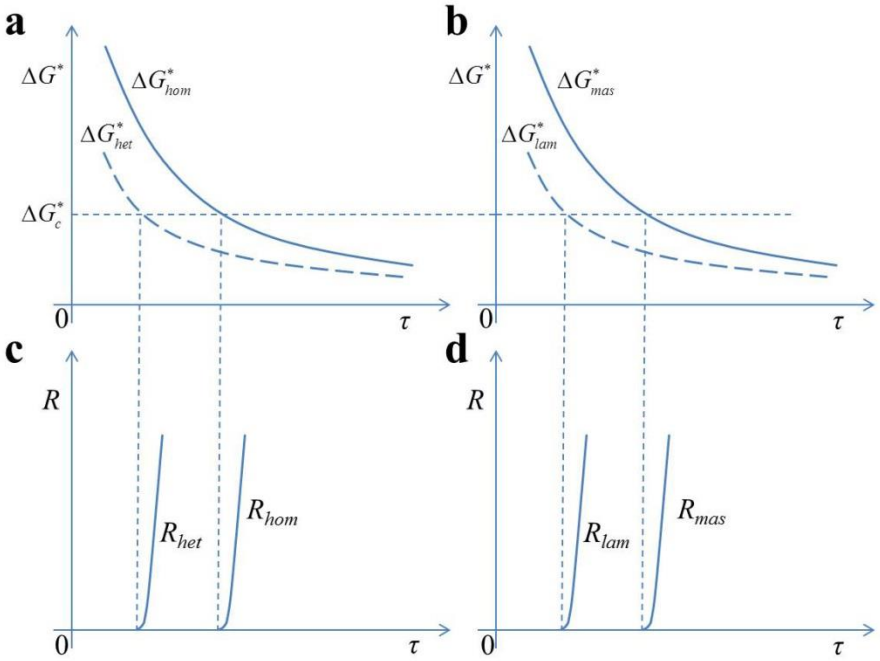

Figure S8. Schematic diagrams of dependences of nucleation energy barrier ΔG^* (a, b) and nucleation rate R (c, d) of γ phase deformation twins on applied shear stress τ for two comparison situations. (a), (c) Comparison between homogeneous and heterogeneous nucleation with the same of the other conditions; (b), (d) Comparison between nucleation in massive and lamellar γ phase with the same of the other conditions. The ΔG_c^* is the critical value of nucleation energy barrier which is necessary for the generation of extensive deformation twins.

Tables

Table S1. Chemical composition (at. %) of each constituent phase in as-cast and annealed Ti-45.5Al-4Cr-2.5Nb alloys examined by EDS method

Sample	Constituent phases	Ti	Al	Cr	Nb
As-cast	γ	44.57±0.62	48.73±0.76	3.34±0.37	3.36±0.28
	B2	45.91±0.27	33.94±1.06	16.91±0.88	3.25±0.078
	α_2	--	--	--	--
S1	γ	47.69±1.17	47.49±1.07	2.32±0.12	2.50±0.12
	B2	53.48±1.09	34.88±1.42	9.01±0.68	2.64±0.03
	α_2	51.43±0.70	41.94±1.01	4.31±0.50	2.33±0.11
S2	γ	48.07±0.58	47.20±0.62	2.27±0.07	2.45±0.13
	B2	54.86±1.16	34.17±0.82	8.24±0.57	2.73±0.02
	α_2	51.54±0.60	42.03±0.46	4.05±0.25	2.38±0.17

Note: Due to the equipment error and adopted data processing method in which two valid digits after the decimal point were reserved for the average value of at least four measurements, the content of elements in constituent phases is equal to 99.99% or 100.01% sometimes.

Table S2. Lattice parameters and weight percentage of each constituent phase in as-cast and annealed Ti-45.5Al-4Cr-2.5Nb alloys achieved by Rietveld refinement to XRD patterns

Sample	γ-TiAl phase lattice parameter (Å)	Weight percentage of γ-TiAl phase (%)	α_2-Ti_3Al phase lattice parameter (Å)	Weight percentage of α_2-Ti_3Al phase (%)	B2 phase lattice parameter (Å)	Weight percentage of B2 phase (%)
As-cast	*a*=4.002 *c*=4.050 *c*/*a*=1.012	87.7	*a*=5.710 *c*=4.627	8.2	*a*=3.161	4.1
S1	*a*=3.995 *c*=4.059 *c*/*a*=1.016	84.4	*a*=5.758 *c*=4.596	13.0	*a*=3.166	2.6
S2	*a*=3.999 *c*=4.061 *c*/*a*=1.016	75.0	*a*=5.719 *c*=4.642	16.9	*a*=3.173	8.1

Note: Due to the diffraction intensity corresponding to η-$TiAl_2$ phase in S2 is very weak, then its Rietveld refinement results aren't included in this table.

Table S3. Room-temperature compressive properties of as-cast and annealed Ti-45.5Al-4Cr-2.5Nb alloys

	Compressive strength σ_c (MPa)	Yield strength $\sigma_{0.2}$ (MPa)	Fracture strain ε_f (%)	Work hardening capacity H_c
As-cast	1617.74	600.10	24.20	1.70
	1385.42	577.40	23.94	1.40
	1421.29	360.85	25.22	2.94
Mean ± standard deviation	1474.82±125.07	512.78±132.07	24.45±0.68	2.01±0.82
S1	2499.20	630.80	41.30	2.96
	2404.89	564.70	32.16	3.26
Mean ± standard deviation	2452.05±66.69	597.75±46.74	36.73±6.46	3.11±0.21
S2	2495.64	608.00	32.50	3.10
	2462.60	688.30	33.00	2.58
	2602.96	642.95	32.79	3.05
Mean ± standard deviation	2520.40±73.38	646.42±40.26	32.76±0.25	2.91±0.29

Here work hardening capacity H_c is defined as $(\sigma_c/\sigma_{0.2})$-1; only two sets of data about compressive properties for sample S1were obtained.

Table S4. Main parameters of γ-TiAl phase used for calculation

the names, symbols and units of parameters	Values
shear modulus G, MPa	7.14×10^4
Poisson's ratio v	0.247
interplanar spacing of twinning phane δ, nm	0.231
moduli of the Burgers vector of twinning dislocation b, nm	0.162
intrinsic stacking fault energy γ, mJ/m^2	64
interfacial energy of incoherent twin boundary σ, mJ/m^2	160

The value of σ is calculated from that of γ, σ=2.5γ here.